

Comparison of LSO and BGO block detectors for prompt gamma imaging in ion beam therapy

Hueso González, F.; Biegun, A. K.; Dendooven, P.; Enghardt, W.; Fiedler, F.; Golnik, C.; Heidel, K.; Kormoll, T.; Petzoldt, J.; Römer, K. E.; Schwengner, R.; Wagner, A.; Pausch, G.;

Originally published:

September 2015

Journal of Instrumentation 10(2015)09, P09015

DOI: <https://doi.org/10.1088/1748-0221/2015/9/P09015>

Perma-Link to Publication Repository of HZDR:

<https://www.hzdr.de/publications/Publ-21965>

Release of the secondary publication
on the basis of the German Copyright Law § 38 Section 4.

Comparison of LSO and BGO block detectors for prompt gamma imaging in ion beam therapy

F. Hueso-González^{a,b1,*}, A. K. Biegun^c, P. Dendooven^c, W. Enghardt^{a,b1}, F. Fiedler^{b2}, C. Golnik^a, K. Heidel^{b2}, T. Kormoll^a, J. Petzoldt^a, K. E. Römer^{b2}, R. Schwengner^{b2}, A. Wagner^{b2} and G. Pausch^a

^a *OncoRay - National Center for Radiation Research in Oncology, Faculty of Medicine and University Hospital Carl Gustav Carus, Technische Universität Dresden, Fetscherstr. 74, PF 41, 01307 Dresden, Germany.*

^b *Helmholtz-Zentrum Dresden - Rossendorf, Institutes of Radiooncology¹ and Radiation Physics², Bautzner Landstraße 400, 01328 Dresden, Germany.*

^c *University of Groningen, KVI-Center for Advanced Radiation Technology, Zernikelaan 25, 9747 AA, Groningen, the Netherlands.*

E-mail: Fernando.Hueso@OncoRay.de

ABSTRACT: A major weakness of ion beam therapy is the lack of tools for verifying the particle range in clinical routine. The application of the Compton camera concept for the imaging of prompt gamma rays, a by-product of the irradiation correlated to the dose distribution, is a promising approach for range assessment and even three-dimensional in vivo dosimetry.

Multiple position sensitive gamma ray detectors arranged in scatter and absorber planes, together with an imaging algorithm, are required to reconstruct the prompt gamma emission density map. Conventional block detectors deployed in Positron Emission Tomography (PET), which are based on $\text{Lu}_2\text{SiO}_5:\text{Ce}$ (LSO) and $\text{Bi}_4\text{Ge}_3\text{O}_{12}$ (BGO) scintillators, are suitable candidates for the absorber of a Compton camera due to their high density and absorption efficiency with respect to the prompt gamma energy range (several MeV).

We compare experimentally LSO and BGO block detectors in clinical-like radiation fields in terms of energy, spatial and time resolution. The high energy range compensates for the low light yield of the BGO material and boosts significantly its performance compared to the PET scenario. Notwithstanding the overall superiority of LSO, BGO catches up in the field of prompt gamma imaging and can be considered as a competitive alternative to LSO for the absorber plane due to its lower price and the lack of intrinsic radioactivity.

KEYWORDS: Instrumentation for hadron therapy; Detector modelling and simulations I; Compton imaging; scintillators; block detector; prompt gamma; in vivo dosimetry.

*Corresponding author.

Contents

1. Introduction	2
2. Motivation	3
3. Aim	4
4. Materials	5
4.1 Scintillator properties	5
4.2 Block detector properties	7
4.3 Electronics and data acquisition	11
5. Experimental setup	11
5.1 Accelerators	11
5.2 Detector setup	12
5.3 Trigger regime	12
6. Methods	13
6.1 Energy calibration	14
6.2 Spatial calibration	16
6.3 Time calibration	17
6.4 Error analysis	18
7. Results and Discussion	18
7.1 Energy resolution	18
7.2 Spatial resolution	19
7.3 Time resolution	22
8. Conclusions	23

This is an author-created, un-copyedited version of an article published in Journal of Instrumentation. IOP Publishing Ltd is not responsible for any errors or omissions in this version of the manuscript or any version derived from it. The Version of Record is available online at <http://dx.doi.org/10.1088/1748-0221/2015/9/P09015>.

1. Introduction

Accelerated protons have been considered since 1946 for cancer treatment [1]. Protons (or heavier ions) stop at a predefined depth inside the tissue, the so called particle range. The dose deposition profile exhibits a maximum (the Bragg peak) close to the ion stopping point, and a fall-off beyond. In principle, ion beam therapy has several advantages over photon therapy:

- *The distal edge*: the dose profile falls steeply beyond the particle range, almost to zero for protons, which is promising for sparing critical organs close to the irradiated tumour.
- *The integral dose*: thanks to the Bragg peak, the dose is focused on the tumour and the damage on healthy tissue is minimised. For photons, the dose in healthy tissue can only be distributed to a larger volume by irradiating from several directions but its integral is higher than for protons.

Main drawbacks are the high costs [2], the lack of evidence about the translation of lower integral dose to clinical outcome [3], and the intrinsic range uncertainties [4]. In ion beam therapy, factors like patient positioning and anatomy changes [5] may yield severe differences with respect to the planned dose, whereas photon plans are much less sensitive in this regard. To circumvent this risk, safety margins are applied and robust treatment plans are designed [6], at the price of an increase of the dose in the healthy tissue compared to the optimum plan.

Notwithstanding the theoretically superior dose conformality of ions, broad safety margins constrain critically the outstanding traits of ion over photon beam therapy and fuel the controversy about the clinical superiority [7, Chapters 2.11-2.13]. The lack of tools for measuring in vivo and in real-time the actual distal fall-off edge, together with the high sensitivity of the ion range to tissue composition, prevent narrower margins. In this context, several groups across the world race towards an experimental device that measures the particle range and dose profile in real-time [8].

Many efforts are focused on prompt gamma rays, a by-product emitted in nuclear reactions along the ion track. The spatial emission distribution correlates with the dose deposition map of the incident ions [9, 10] and provides an indirect measurement of the particle range. Passive collimation with a pin-hole [11], parallel slit [12] or multi-slit [13] are promising approaches for clinical systems based on Prompt Gamma Imaging (PGI). Recent experiments have demonstrated the feasibility of real-time millimetre range verification with a knife-edge slit collimator [14] at clinical beam intensities [15] and with heterogeneous phantoms [16].

An alternative PGI system is the Compton camera, which comprises multiple position sensitive gamma ray detectors arranged in one or more scatter planes, and one absorber plane. The energy deposited by the prompt gamma rays in each plane as well as the point of interaction is measured. Based on the well-known Compton formula [17], an iterative imaging algorithm reconstructs the prompt gamma ray emission density map. In contrast to a slit camera, no mechanical collimation is needed in order to reconstruct the angle of incidence of the gamma ray, and two-dimensional (2D) or even three-dimensional (3D) images instead of one-dimensional (1D) profiles are obtained.

On the other hand, the instrumentation and detector requirements in terms of spatial, time and energy resolution are much higher for a Compton camera, and the reconstruction algorithm is more difficult and computationally intensive. Nowadays, a PGI Compton camera prototype

demonstrating range verification in a clinical scenario is still a challenge several institutes aim at [18, 19, 20, 21, 22, 23, 24]. Technical complexity, electronic expense, low coincident efficiency, high gamma ray flux (detector load), radiation background and the elevated percentage of random coincidences are intrinsic hurdles that cast doubts on the applicability of this technique.

2. Motivation

The imaging of the prompt gamma rays produced by a clinical proton beam represents an experimental challenge due to the following factors:

- The broad and polychromatic energy spectrum up to 10MeV (range of interest lies between 1 and 6MeV) [25].
- The high instantaneous production rate of about 10^9 gamma rays per second [26], emitted within a spatial region on the 20cm scale and in all directions.
- The large radiation background due to neutrons, scattered charged particles and material activation [27].

Several experimental PGI systems have been proposed and designed in the recent years. Among these, the Compton camera has probably the highest requirements concerning detectors, electronics and data processing. It is important to choose detector materials that adapt to this specific environment and cope best with the constraints mentioned above. Diverse theoretical studies and simulations about the geometry and material choice of a Compton camera for PGI have been published in the last years [28, 29, 30]. The prerequisites of a camera comprising (for simplicity) two layers are:

- An excellent energy resolution is mandatory to accurately calculate the scattering angle θ of the incident gamma ray by means of the Compton equation. This defines a cone of response with opening angle θ . If the incident gamma ray energy is known, it is enough to have a good energy resolution in the scatterer. Otherwise, this requirement applies also to the absorber.
- A high spatial resolution is needed for placing the Compton cone vertex in the 3D space and orientating its axis.
- A good timing resolution is advisable for filtering out false coincidences due to the high rate of (non-prompt) background in the clinical environment.
- A high absorption efficiency (density as well as effective atomic number) is needed in the absorber to fully stop the prompt gamma rays, which have an energy up to 6MeV, to minimise the effect of escape energy (incomplete energy deposition) in the reconstruction.
- A trade-off between energy resolution and absorption efficiency. As the prompt gamma spectrum is not monoenergetic, the absorber requires in principle a high energy resolution (see above). However, as the energy range is high, Compton scattering predominates over photoabsorption and scattered gamma rays may escape the detector with moderate probability. Hence, it may be of greater importance to use very dense (or thick) materials, as a high energy resolution is wasted anyway if there is missing energy.

- The material should be radiation hard to sustain the high rates and damage due to secondary particles (neutrons, charged particles).
- To cope with the high expected radiation rate, scintillation detectors with very long decay times or large afterglow are not advisable.
- Intrinsic radioactivity of the material is a drawback as it can lead to false coincidences.
- Non-hygroscopic materials are preferred to avoid scattering in the sealing.
- Concerning clinical implementation, the camera should be placed at ~ 30 cm distance from the beam axis and have a low footprint in order to minimise the interference with the patient and medical staff. Furthermore, a compromise between camera size (higher sensitivity) and affordable price (commercial applicability) has to be reached.

Taking into account these numerous requirements, the block detectors from standard PET scanners [31], based on $\text{Lu}_2\text{SiO}_5:\text{Ce}$ (LSO) and $\text{Bi}_4\text{Ge}_3\text{O}_{12}$ (BGO), are straightforward candidates for the absorber plane. They are well known detectors, non-hygroscopic, fast and radiation hard [32, 33]. Furthermore, their absorption efficiency is high due to their density and effective atomic number, and the energy, spatial and timing resolution are good.

Textbook knowledge related to PET scanners [31], where the gamma ray energy is limited to 511 keV, is that LSO pixellated detectors have gained importance to the detriment of cheaper BGO due to a better performance concerning energy, spatial and time resolution, mainly due to its four times higher light yield (number of scintillation photons per MeV) and much shorter decay time. Several studies comparing the different performance of BGO and LSO for PET [34, 35, 36, 37] have been published.

Is this prior experience enough to discard BGO as absorber of a PGI Compton camera? How does the increased gamma ray energy affect the detector performance? Does the four times higher cost of LSO crystals [38, p. 64] match also in the PGI scenario with the boost in performance compared to BGO? Whether or not the higher energies (and thus number of scintillation photons) will suffice for considering BGO as a competitive alternative to LSO is the essential question that motivates this paper. To answer it, experiments to characterise the different block detectors in clinical-like radiation fields are mandatory.

3. Aim

To compare the performance of BGO and LSO scintillators for range verification as part of a PGI clinical system, namely as absorber of a Compton camera, benchmark experiments are conducted at several research accelerators. They provide a photon radiation field similar either in the energy range and/or timing structure with the one expected in a clinical pulsed accelerator [39]. BGO and LSO detectors are compared specifically in terms of energy, spatial and time resolution. Factors like absorption efficiency, intrinsic activity, and cost-effectiveness ratio are also addressed.

The experimental results at these measurement campaigns expand and complement the theoretical predictions and simulations performed already in this field. The suitability of BGO as an alternative to LSO as absorber choice of a Compton camera aiming at PGI is discussed.

Material	LSO	BGO
Mass density ρ (g/cm ³)	7.40	7.13
Melting point MP (° C)	2050	1050
Molière radius R_M (cm)	2.07	2.23
Radiation length X_0 (cm)	1.14	1.12
Nuclear interaction length λ_I (cm)	20.9	22.8
dE/dx per mip (MeV/cm)	9.6	9.0
Effective atomic number $Z_{\text{eff}} \pm 1$	66	75
$\rho Z_{\text{eff}}^4 \times 10^{-6} \pm 10$ g/cm ³	140	230
$\rho Z_{\text{eff}}^2 \times 10^{-3} \pm 3$ g/cm ³	32	42
$\rho Z_{\text{eff}} \pm 20$ g/cm ³	490	560
Light yield (LY) (% NaI)	85	21
$d(LY)/dT$ (%/° C)	-0.2	-0.9
Rise time (ps)	~ 30	~ 30
Decay time (ns)	40	300
Peak excitation $\lambda_{\text{exc}} \pm 1$ nm	358	304
Maximum emission λ_{max} (nm)	402	480
Cut-off transmission ± 5 nm	390	315
Index of refraction n	1.82	2.15
Photofraction @ 511 keV (%)	34	44
Energy FWHM @ 662 keV (%)	8	9
Afterglow (%/ms)	< 0.1/6	0.005/3
Internal activity (Bq/cm ³)	~ 280	0
Hygroscopic	No	No
Price in year 2010 (\$/cc)	40	9

Table 1. Comparison of basic properties of the LSO and BGO scintillation materials. Data are extracted from [31], [42, p. 345], [43, 44, 45, 46] and [47, p. 55]. *mip* refers to minimum ionising particle. Note that the prices given for crystals are rough estimates [38, p. 64] based on a comparison of detector costs. They are of course affected by the actual market situation.

4. Materials

At OncoRay and Helmholtz-Zentrum Dresden-Rossendorf (HZDR), various Compton imaging detector setups are under evaluation [40, 41]. The absorber comprises PET block detectors (from commercial scanners) based on LSO and/or BGO scintillators. These are tested individually at several research accelerators for comparing their performance as absorber.

4.1 Scintillator properties

Table 1 summarises the main properties of LSO and BGO scintillation materials. Figure 1 depicts the attenuation coefficient of photons with the material for the different interaction mechanisms. Based on these literature reference values, we can draw some conclusions concerning the intrinsic potentials of each scintillator:

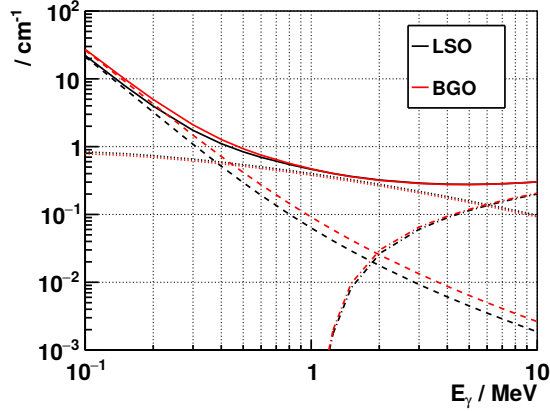


Figure 1. Comparison of the photon attenuation coefficients μ (cm^{-1}) of the LSO and BGO scintillation materials as a function of the photon energy E_γ for the three main interaction mechanisms: photoelectric absorption (dashed line), Compton scattering (dotted line) and pair production (dash-dotted line), and the total attenuation without coherent scattering (solid line). Data are extracted from [43] for Lu_2SiO_5 and $\text{Bi}_4\text{Ge}_3\text{O}_{12}$, and multiplied by the respective material density.

- Both LSO and BGO materials are non hygroscopic, very dense, have a very low Molière radius and a high effective atomic number Z , thanks to Lu ($Z = 71$) and Bi ($Z = 83$), respectively. Hence, they are suited as absorber. The absorption efficiency of BGO is higher at energies under 1 MeV (dominated by the photofraction): its lower density is counterbalanced by its larger Z compared to LSO. For 511 keV photon energy, the total attenuation (without coherent scattering) is 0.82 cm^{-1} for LSO and 0.91 cm^{-1} for BGO; the photoelectric attenuation coefficient is 0.28 cm^{-1} versus 0.40 cm^{-1} , i.e. $\sim 40\%$ larger for BGO. At energies above 1 MeV, where Compton scattering predominates over the photoelectric effect (one order of magnitude), the total attenuation factors (and also the incoherent scattering and pair production coefficients themselves) are more or less equal for LSO and BGO. At 4 MeV, the pair production is half the Compton attenuation coefficient; above 6 MeV, the first predominates over the latter. The residual photoabsorption efficiency is still $\sim 40\%$ higher for BGO.
- LSO has a high internal beta and gamma ray activity in the energy range below 1 MeV. This does not overlap with the prompt gamma energy range, but increases the chance of false coincidences (see next subsection) as well as pile-up with true events. The afterglow of LSO is higher than for BGO [48]. On the other hand, its decay time is much shorter than the BGO one, so that the sustainable detector rate is higher and the overall pile-up probability decreases (assuming common detector sizes).
- The energy resolution of LSO is better, especially for the low energy range, mainly due to the statistical contribution (scales with the number of scintillation photons as $N_{\text{ph}}^{-1/2}$) according to the four times higher light yield [49]. The lower light self-absorption of BGO [35] plays a minor role.
- The time resolution of a detector made of BGO or LSO is affected by the rise and decay time of the light pulse, and the light yield. LSO is expected to have a much better time resolution

than BGO, at least when coupling the crystal with standard photomultiplier tubes and analogue discriminators. The low afterglow and a relatively small but fast (60ns) component of the BGO decay time [50] may notably enhance its time resolution. Still, LSO is expected to allow a better background suppression for PGI in a clinical pulsed accelerator thanks to its better time resolution. The much shorter decay time compared to that of BGO accounts for lower pile-up probability (better count rate performance), even taking into account larger afterglow and the high internal radioactivity.

- The complex intrinsic radiation background of LSO shows a broad energy spectrum below 1 MeV and stems from ^{176}Lu β^- decay (most electrons are stopped inside the material) and simultaneous gamma ray cascade of 307, 202 and 88 keV (photons may escape the material with a moderate probability) [51].
- The intrinsic spatial resolution, assuming that the interaction is a photoelectric effect, depends on the range of the photoelectron. For the PGI energy range, LSO has a slightly shorter electron range, around 5 % less [52] (which is almost irrelevant, as it could be balanced e.g. by a 5 % larger pixel size in BGO). Note that the Continuous Slowing Down Approximation (CSDA) range of 4 MeV photoelectrons is around 4 mm, which indicates a constraint of the minimum crystal pitch. Anyway, at these energies, the photoelectric absorption is a rather infrequent process (2 % absolute photopeak efficiency for 2 cm thick BGO) compared to incoherent scattering (29 %) or pair production (8 %). In case of a Compton effect, the same conclusions regarding the recoiling electron could apply. If the scattered gamma ray escapes the detector, the intrinsic spatial resolution will not be affected but there will be missing energy affecting the reconstruction algorithm. If the scattered gamma ray is fully absorbed in subsequent processes in the same pixel, there will not be any escape energy, the spatial resolution is not compromised, but the energy resolution can be affected by non-linearities (see next point). The same observations apply in case of pair production, depending on the subsequent absorption of the two annihilation photons.
- Non-linearity effects: a light yield that varies with the energy leads to a non-proportional response spectrum [53]. This degrades the energy resolution when a photon suffers multiple interactions in the crystal until being fully absorbed. This intrinsic contribution to the energy resolution does not differ too much between LSO and BGO [35, 49, 54] in contrast to the statistical one.

In summary, LSO outperforms BGO especially in the light yield and thus on the energy, spatial and time resolution, whereas BGO has much lower price, no internal activity and a better photoabsorption efficiency (a distinguishing feature at 511 keV or lower photon energies, where the photoelectric effect is dominant).

4.2 Block detector properties

A block detector is a square matrix of segmented or pixellated scintillating crystals coupled to four light-sharing PhotoMultiplier Tubes (PMTs), as depicted in figure 2. The essential feature is the capability to retrieve the pixel where the gamma ray interacts based on the ratio of light collected

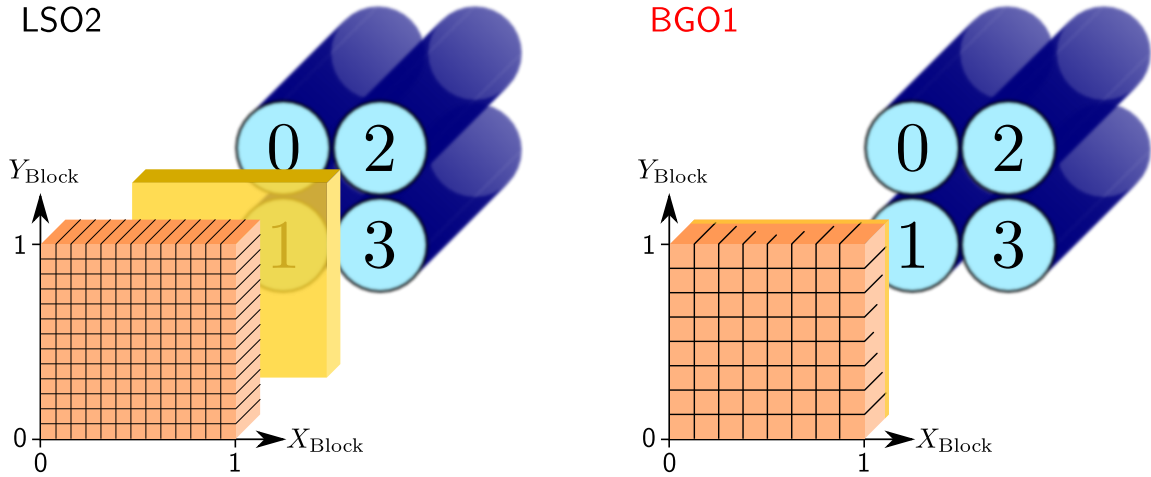


Figure 2. Sketch of the LSO2 (left) and BGO1 (right) block detectors with the PMT numbering convention and crystal coordinate system, namely the X_{Block} and Y_{Block} axis (relative position between 0 and 1). Crystals are depicted in orange, PMTs in blue and the light guide in yellow. The actual detector size is given in table 2. The labelling convention of the individual pixels of the square matrix $[i, j]$ is: $[0, 0]$ for the pixel at $X_{\text{Block}} = 0, Y_{\text{Block}} = 0$; i and j increase with X_{Block} and Y_{Block} , respectively. Taking BGO1 as example, the edge pixel $[0, 7]$ is at $X_{\text{Block}} = 0, Y_{\text{Block}} = 1$.

by each PMT. The block detectors used in this study and their properties¹ are listed in table 2. We name them as LSO2 and BGO1. We refer to these names when speaking about the concrete detector results, in contrast to LSO and BGO for general features of the scintillation materials.

Detector name	LSO2	BGO1
Active volume (mm×mm×mm)	52.7 × 52.7 × 20.0	52.7 × 52.7 × 20.0
Granularity	Independent pixels	Segmented crystal
Pixel matrix	13 × 13	8 × 8
Crystal pitch (mm×mm×mm)	4.0 × 4.0 × 20.0	6.4 × 6.4 × 20.0
Light guide	Coupled to block	Cut into block [46]
Operating voltage	+900V	+1350V
Commercial scanner	Biograph PET/CT	ECAT EXACT 47 PET

Table 2. Comparison of the properties of the different block detectors from Siemens Medical Solutions USA, Inc. Molecular Imaging Division, whose sketch is depicted in figure 2. Spatial dimensions are given as height × width × depth.

Are the conclusions drawn in subsection 4.1 concerning the expected resolution of the different scintillation materials still valid for segmented or pixellated crystals such as block detectors?

- The energy resolution is strongly affected by the spatial resolution. The reason is that different pixels (crystals) have a distinct coupling to the PMTs, reflection loss and scintillation light sharing ratio. Different regions of the photocathode are illuminated depending on the pixel and the response may not be uniform (particularly for edge pixels). In order to obtain

¹Siemens Healthcare Molecular Imaging, private communication.

a good energy resolution, each pixel has to be calibrated separately to adjust for offset and gain (to correct the different response, in the sense of different sum signal of the four PMTs depending on pixel position for the same energy deposit). Prerequisite is therefore to be able to resolve each pixel. Accordingly, if BGO1 pixels are separated worse, an individual energy pixel spectrum will be mixed with neighbour ones and the energy resolution will be degraded.

- The time resolution may also be affected pixel-wise if the PMT high voltages and gains are not close enough to each other. The PMT transit time links to the operating voltage, whereas the energy threshold and time walk depend on the PMT and preamplifier gain. A separate trigger on each PMT (instead of a global detector trigger) is needed in order to correct for different PMT transit times or time walk.
- The spatial resolution is mainly affected by the ability of resolving neighbour pixels in the crystal decoding map (flood map). Assuming a perfect discrimination capability, the lower limit for the spatial resolution is the crystal pitch ($4\text{ mm} \times 4\text{ mm}$ for LSO2). The intrinsic contribution of the photoelectron CSDA range, below 5 mm [52], to the spatial resolution is minor compared to the Poissonian statistical noise (and the effect of multiple processes, see below). The gamma ray interaction point is recovered from the ratio of scintillation photons collected at each separate PMT. As LSO has a higher light yield, the relative statistical noise is lower and the pixels can be resolved better from each other [31]. In other words, for an equal detector size and acceptable pixel discrimination, LSO based detectors can comprise more pixels per block than BGO, e.g. 169 compared to 64 for standard PET scanners. As the LSO2 crystal pitch is smaller than for BGO1, the spatial resolution is better. Note, however, that one could build a BGO 8×8 block detector with $4 \times 4\text{ mm}^2$ crystals, to match the same resolution. Thus, the limitation of BGO is in the number of pixels per block rather than in the spatial resolution itself. Indeed, high resolution PET scanners can be also based on BGO as its higher photofraction reduces the inter-crystal scattering for equal crystal pitch [55].

For these reasons, LSO has gained importance to the detriment of BGO in the PET environment. However, in the PGI environment, where the energy range of interest is over 2 MeV, the number of scintillation photons in a typical event is at least four times higher than in the PET scenario, and the four times lower light yield of BGO might not be a severe drawback concerning the block detector performance.

Furthermore, LSO has a larger afterglow and high intrinsic radioactivity, around 15 kcps per block detector, with a simultaneous β^- decay and gamma ray cascade (see previous subsection). This inherent background might have the following consequences concerning its use in a Compton camera:

- Pile-up of true events with intrinsic radiation (minor effect).
- Random coincidences: β^- event in the absorber and Compton effect of a true prompt gamma ray in the scatterer. This can be minimised if the time resolution of scatterer as well as absorber is excellent, or if the energy filter of the absorber is set at high energies.

- Trojan coincidences: a β^- interaction in the absorber, a photon of the cascade escaping it and reaching the scatterer. These events are simultaneous and can not be rejected based on timing measurements, only by applying appropriate energy and Compton kinematics filters.
- The aforementioned problems scale with the size of the Compton camera. An absorber based on 100 LSO block detectors leads to a global background of 1.5 Mcps and discriminating in real-time false coincidences poses a serious challenge. The same applies if one enlarges the detector size instead of increasing the number of detectors, with the additional drawback of higher pile-up probability.

One could argue that, as the range of interest of prompt gamma rays is over 2 MeV, the intrinsic radioactivity of LSO (under 1 MeV) can be easily rejected with a high energy threshold on the LSO detector (arming circuit). However, this strategy is misleading and has a huge impact on the efficiency of the Compton camera. The reason is that the energy filter can only be set on the energy sum (scatterer and absorber) but not on the individual detectors. For example, events with large scatter angles deposit a high energy in the scatterer and low in the absorber. Thus, individual discriminator threshold has to be low on all stages of the camera, and coincident events have to be filtered based on the energy sum. Otherwise, a high individual energy threshold biases the type of events (gamma ray directions) that the camera registers.

A comment should be added regarding the spatial resolution. For 4 MeV prompt gamma rays, direct photoabsorption is unlikely, cf. figure 1. Rather, multiple interaction processes can take place in the same detector until absorbing the whole energy. If Compton scattering or pair production is followed by photoabsorption (of the scattered gamma ray or annihilation photons) in neighbour pixels, the spatial information of this event is degraded, as neither the detector design nor the modified Anger logic are thought for multiple hits. This has also an effect on the measured energy, which is calibrated independently for each pixel. On the other hand, if the secondary photons escape the detector, the spatial information will not be jeopardised, but the energy of the scattered gamma ray and thus the opening angle of the Compton cone is biased (provided that the gamma ray energy is not known in advance).

The complexity and variety of this type of processes can only be covered by Monte Carlo simulations that include an accurate detector model. However, this exceeds the scope of this paper. From a qualitative point of view, we can intuit that these multiple interaction processes will be equally common in LSO as well as BGO due to their similar Compton scattering and pair production attenuation coefficient at 4 MeV, and BGO will absorb better the secondary photons due to its higher photofraction over the whole energy range.

Altogether, multiple interactions in the same pixel until full absorption are acceptable events, if in different pixels then it leads to false events (to be treated as background), and single interactions with escape energy lead to valid spatial information but energy-biased events (which the reconstruction algorithm may however handle). The scientific community is aware about the limitation of a two-layer Compton camera with photons of unknown and very high energy, where the photoabsorption is rather rare, and has evaluated by means of simulations the noise introduced in the reconstructed images by different type of interactions [56]. Alternatively, three-stage (or more) Compton cameras, which do not require a full absorption, have been proposed and are under development [57, 20].

Accelerator name	ELBE	AGOR	C230
Location	HZDR	KVI-CART	OncoRay
Accelerator type	Superconducting LINAC	Superconducting cyclotron	Isochronous cyclotron
Accelerated particles	Electrons	Protons	
Used beam current	~ 1 nA	~ 10 pA	~ 50 pA
Kinetic energy	12.5 MeV	150 MeV	100 MeV
Bunch frequency f_{bunch}	13 MHz	55 MHz	106 MHz
Bunch width	~ 5 ps	~ 400 ps	~ 2 ns
Target material	Nb	Graphite	PMMA
Target size	2 μm foil	10 cm \times 10 cm \times 30 cm	5 cm \times 5 cm \times 10 cm
Gamma radiation field	Continuous	Continuous + Characteristic	
Gamma ray energy range	≤ 12.5 MeV	$\lesssim 8$ MeV	
Detected gamma ray flux	10^5 s^{-1}	10^5 s^{-1}	$5 \times 10^4 \text{ s}^{-1}$
Production process	Prompt bremsstrahlung photons	Prompt nuclear reactions	
Background fraction	Very low	High: Neutrons, material activation	
Measurement campaigns	11/2012, 11/2013	07/2013	02/2015
Scintillators used	LSO2, LSO2-BGO1	LSO2-BGO1	BGO1
Rationale	Timing, spatial at high energies	Test at research facility	Test at clinical scenario

Table 3. Comparison of the characteristics of the gamma radiation field produced at the three different accelerators. Note that the table presents the parameters set up in our particular experiments. The LSO2 detector is also used in [40], the BGO1 in [41]. PMMA refers to polymethyl methacrylate.

Concerning the size of the block detectors, which are optimised for PET energies, one may think of increasing their thickness when applied to PGI. For example, in order to attenuate 70% of the incoming 4.44 MeV gamma rays, the detector thickness should be 4 cm instead of 2 cm.

Another remark is that the difference in the scintillator price (cf. table 1) could play only a minor contribution with regard to the overall system costs if these are dominated by e.g. the assembly or electronics.

4.3 Electronics and data acquisition

The readout electronics varies only slightly between the different measurement campaigns, and is based on CAEN (Viareggio, Italy) VERSAModule Eurocard bus (VME) front-end modules. The software for data acquisition is a custom multi-threaded application developed on the ROOT framework (CERN) [58], which provides real-time control of the VME modules and on-the-fly data analysis with graphical feedback. The energy deposit and trigger time stamp is monitored live for each detector. The details about the analogue electronics and data acquisition system are described in [40].

5. Experimental setup

5.1 Accelerators

The detectors described in table 2 are tested at the linear electron accelerator (ELBE) of HZDR^b [40], at the superconducting cyclotron (AGOR) of KVI-CART^c [59] and at the clinical isochronous cyclotron (C230) of OncoRay^a.

The setup and beam settings at each of these research accelerators are compared in table 3. These facilities are appropriate for characterising the detectors in a radiation field with similarities to the clinical scenario.

ELBE electron accelerator is used to provide bunched bremsstrahlung photons with a maximum energy of 12.5 MeV. A comprehensive description of the facility is given in [60]. It is a good testing platform for the block detectors concerning timing resolution as well as spatial resolution for different photon energy ranges:

- In a clinical proton cyclotron, the emitted prompt gamma rays are also bunched with the accelerator frequency, namely 106 MHz for the C230 [39] compared to the 13 MHz at ELBE [40].
- The energy range of the bremsstrahlung photons is comparable to the one expected for prompt gamma rays in a clinical proton beam (several MeV) and allows testing detectors in an energy range not accessible using common radioactive sources.
- The electron bunch width [60] is about 5 ps, in contrast to $\gtrsim 300$ ps proton bunch spread [26] in the C230, thus allowing an intrinsic detector time resolution measurement.

AGOR is a superconducting cyclotron, which provides bunched protons (and other ions) with energies up to 190 MeV. In our experiment, we use a fixed energy of 150 MeV. A detailed description of this accelerator is given in [61]. It has many similarities to the clinical proton cyclotron and is therefore indicated to test all properties of the block detectors with phantom experiments:

- In a clinical proton cyclotron, the emitted prompt gamma rays are also correlated to the accelerator frequency: 106 MHz for the C230 compared to the 55 MHz at AGOR for 150 MeV protons.
- 150 MeV is a relevant proton energy in clinical therapy, and the nature of prompt gammas and background ratio is comparable to the conditions in the clinical environment.

C230 (Cyclone[®] 230) is a clinical proton cyclotron of IBA (Louvain-la-Neuve, Belgium) present at OncoRay. The experimental area at this center, comprising a horizontal fixed beam line, resembles best the clinical irradiation conditions.

5.2 Detector setup

The detector setup is described in figures 3 and 4.

5.3 Trigger regime

- At ELBE, the electron current is adjusted in order to produce a flux of 10^5 bremsstrahlung photons per second (detector trigger rate), which are forward focused. Each block is measured separately as standalone setup covering the whole beam spot.
- At AGOR, both LSO2 and BGO1 are used simultaneously as part of a Compton camera setup, but with individual trigger on each block (no coincidence conditions). The trigger rate at each block, which is placed ~ 30 cm away from the center of the target (beam axis), is around 10^5 s⁻¹.
- At C230, the BGO1 block is tested individually (no majority conditions). It is placed about 25 cm away from the target and the measured rate is about 5×10^4 s⁻¹.

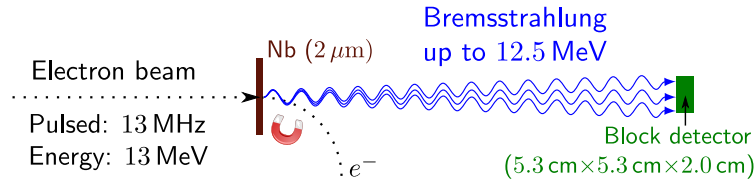


Figure 3. Experimental setup at the ELBE accelerator. Electrons (dotted arrow) accelerated up to a total energy of 13 MeV in 13 MHz bunches – corresponding to 77 ns bunch separation – interact with atoms of a Niobium foil. Bremsstrahlung photons (continuous spectrum up to 12.5 MeV) are radiated promptly (and forward-focused) as a result of the deflection of the electrons by the electric field of the nuclei, and are registered by the block detector.

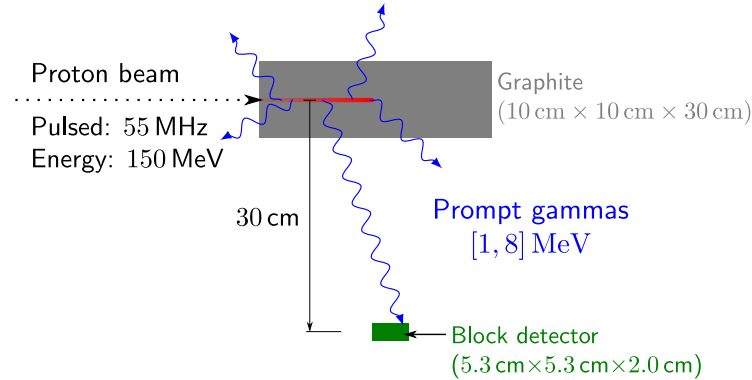


Figure 4. Experimental setup at the AGOR accelerator. Protons (dotted arrow) with 150 MeV kinetic energy in 55 MHz bunches – corresponding to 18.2 ns bunch separation – penetrate into a graphite target. As a result of nuclear interactions, gammas are radiated promptly (continuous and characteristic spectrum [62]) in 4π and measured by the block detector (dynamic range up to 8 MeV). At the C230 accelerator, an analogous experiment is performed with a proton energy of 100 MeV in 106 MHz bunches, a PMMA target and a detector distance of 25 cm to the beam axis.

Although the energy range of interest for prompt gamma rays is above 2 MeV, the discriminator threshold at each detector has to be kept low because valid Compton events may deposit also small energies in the absorber. Coincidences have to be built based on the trigger time and a 2 MeV energy sum threshold can be then applied in the data processing software.

6. Methods

An extended calibration procedure for block detectors is mandatory to obtain a good energy, spatial and time resolution. The main steps are enumerated below and detailed in the corresponding subsections.

- The four PMT output channels are recorded by a charge to digital converter.
- Different gain and signal offset of each PMT are corrected by matching the spectrum shape.
- A preliminary energy calibration is carried out for each corrected PMT spectrum.
- The crystal decoding map, also known as flood map, is generated.

- The flood map is segmented in regions corresponding to each pixel.
- Energy sum spectra are drawn for each pixel and recalibrated to account for the pixel-dependent light coupling. The dependence of the pulse height distribution on the interaction position is a well-known effect in detectors based on Anger logic.
- Time spectra for each pixel are corrected for transit time effects between PMTs.
- Global time spectrum is corrected for energy dependent time walk.

6.1 Energy calibration

For the energy calibration, a measurement with a radioactive source like ^{22}Na or ^{60}Co , at a distance large enough to ensure a (more or less) homogeneous irradiation of all pixels, is performed. Note that the discriminator threshold should be similar for all PMT channels. The procedure is divided in two steps:

1. **PMT gain and offset adjustment.** As the irradiation is homogeneous, the histogram of the charge recorded by the charge to digital converter (QDC), cf. figure 5 (left), should have the same shape for each PMT (except for an offset and gain factor). A custom software tool, named as *HistStretcher*, allows the overlap of histograms and interactive adjustment of the histogram offset and gain. Thanks to the graphical real-time feedback, one can refine until the four spectra match in shape, as seen in figure 5 (right). The difference in gain between channels is already small at figure 5 (left), as we adjust the PMT voltage through the rear panel of the block detector, which provides four plastic screws regulating the voltage division at each tube. These screws are adjusted iteratively so that the width of the distributions (in channels) is more or less similar, and the remaining differences are corrected by the aforementioned gain matching.

A provisional energy calibration of the corrected histograms is performed empirically. As the scintillation light of each event is shared between the four PMTs and this ratio and the light coupling vary from pixel to pixel, one should not expect to see a photopeak in these histograms (if all pixels are irradiated). But this does not mean that this preliminary calibration is done blindly. The guideline is the energy sum spectrum, namely the event-wise sum of the four calibrated channels of figure 5 (right). The calibration can be retuned until the resulting sum spectrum, cf. figure 6 (left, no spatial filters), lies roughly in the expected energy range and the pedestal is located at 0 MeV. From these calibrated histograms, the crystal decoding map can be calculated (see subsection 6.2). One has to keep in mind that, rather than providing the final energy calibration, the goal of this step is to compensate for the different gain (and offset) of each tube and to obtain a symmetric flood map with a clear separation between pixels, a precondition for the next step.

2. **Energy calibration of the individual pixels.** After the spatial calibration of the flood map is performed, we can draw the energy sum spectrum of the detector for different spatial regions (pixels), as depicted in figure 6 (left). One can see that the selected pixel spectra have a similar shape but different offset or gain (as before), due to the distinct light coupling.

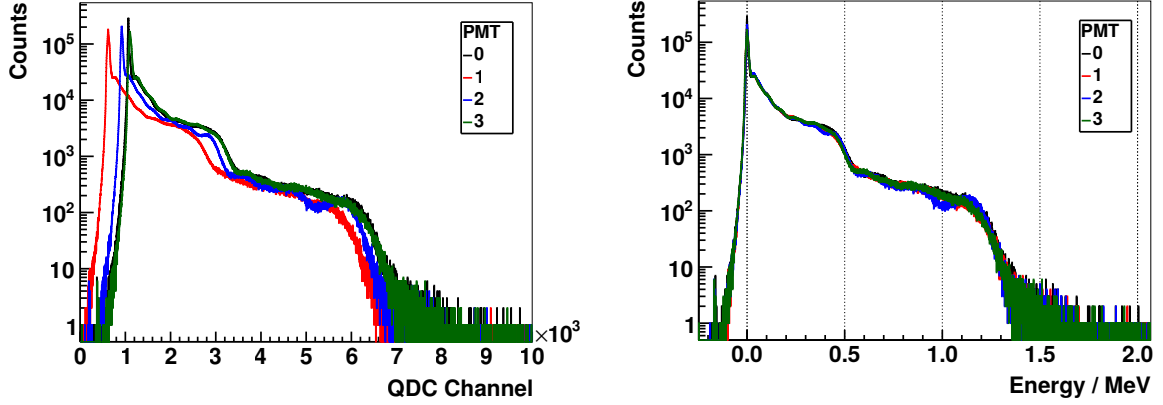


Figure 5. Left: response spectrum of the four PMTs of the BGO1 detector when irradiated with a ^{22}Na source. Right: calibrated energy spectra after regulating offset and gain to match their shapes. Vertical scale is chosen arbitrarily.

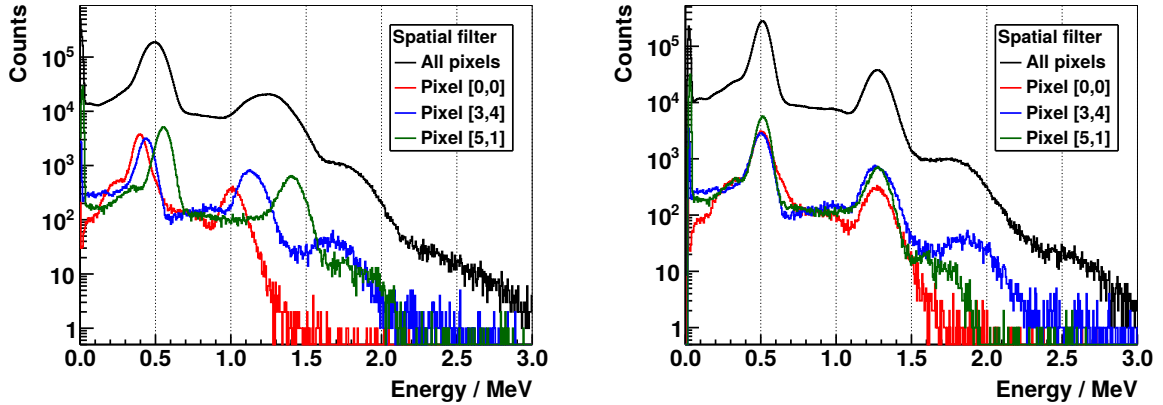


Figure 6. Left: event-wise sum of the energy recorded at each PMT of the BGO1 detector, as depicted in figure 5 (right). Different energy spectra depending on the spatial cuts are superimposed. Right: event-wise energy sum after pixel-wise recalibration of the energy spectra of the left plot.

In order to correct for this additional effect, separate energy spectra are drawn for every pixel and individually recalibrated with an automatic template matching procedure. The *HistStretcher* software tool allows refining by hand the automatic procedure, as the shape of the energy spectra of edge pixels differs significantly from the rest. The result of this recalibration is shown in figure 6 (right).

The energy information is relevant for analysing the photopeak resolution for discrete gamma ray lines. In principle, the energy resolution is different for each pixel, but a global detector resolution can also be obtained by summing up all pixel regions, cf. figure 6. Apart from that, the energy scale is valuable for characterising the spatial and timing resolution for different ranges of interest:

- PET range: $[0, 1]$ MeV. This covers the typical energy region of 511 keV photons created by the annihilation of positrons with electrons (PET imaging). Standard block detectors from medical PET scanners are well characterised and optimised for these energies. This energy range is accessible with common radioactive sources.

- Middle range: $[1, 2]$ MeV. This intermediate range is above the typical energies at PET imaging, but is still accessible with radioactive photon sources.
- PGI range: ≥ 2 MeV. It is the range of interest in PGI due to characteristic prompt gamma lines with a strong correlation with the particle range [25]. This region is not accessible by means of common radioactive sources.

As the block detector is employed in the Compton camera as absorber (high energy deposit), the middle and high range are of special interest. It is worth to note that the energy scale, labelled as *Energy* for the sake of clarity, does not refer to incident photon energy but to the energy deposit in the detector. The vertical axis of all histograms is chosen arbitrarily and is labelled as *Counts*.

6.2 Spatial calibration

The flood map of the pixellated or segmented block detector can be obtained from the relative intensities measured at the four light-sharing PMTs (figure 2): the modified Anger logic. The standard center of gravity equation [63] is used for calculating the relative crystal coordinates $X_{\text{Block}} \in [0, 1]$, $Y_{\text{Block}} \in [0, 1]$:

$$X_{\text{Block}} = 0.5 + 0.5 \times \frac{E_2 + E_3 - E_0 - E_1}{\sum_{i=0}^3 E_i} \quad (6.1)$$

$$Y_{\text{Block}} = 0.5 + 0.5 \times \frac{E_2 + E_0 - E_3 - E_1}{\sum_{i=0}^3 E_i} \quad (6.2)$$

where E_i is the (calibrated) energy measured at the channel (PMT) i , cf. figure 5 (right).

The crystal decoding map is drawn and divided into crystal regions corresponding to each pixel. This segmentation is done automatically with the neighbour standard deviation algorithm [64]. The result can be seen in figure 7 (right). Energy and time histograms are then drawn for each of the regions separately for a refined pixel-wise recalibration.

Distortion correction In general, the flood map of block detectors does not exhibit a uniform distribution of pixels. The reason is the proportional response (center of gravity equation) assumed by the modified Anger logic, which neglects non-linear effects. As a result, a distorted map is generated with the so-called pincushion shape, see figure 7 (left). This shape is especially pronounced for the LSO2 detector: all pixels are independent (it is not a segmented crystal like BGO1) and a guide distributes all the scintillation light to the four PMTs. In some cases, before performing the automated segmentation, we apply a distortion correction [65] to recover a more uniform and squared shape. The parameters of this algorithm have to be adjusted empirically. Note that we do not aim at a perfect uniform pixel distribution, as the pixel identification is not done with a rectangular grid but with the segmentation method. Still, the distortion correction optimises the outcome of the segmentation method, particularly for the edge pixels, which are compressed in very few bins, cf. figure 7 (left).

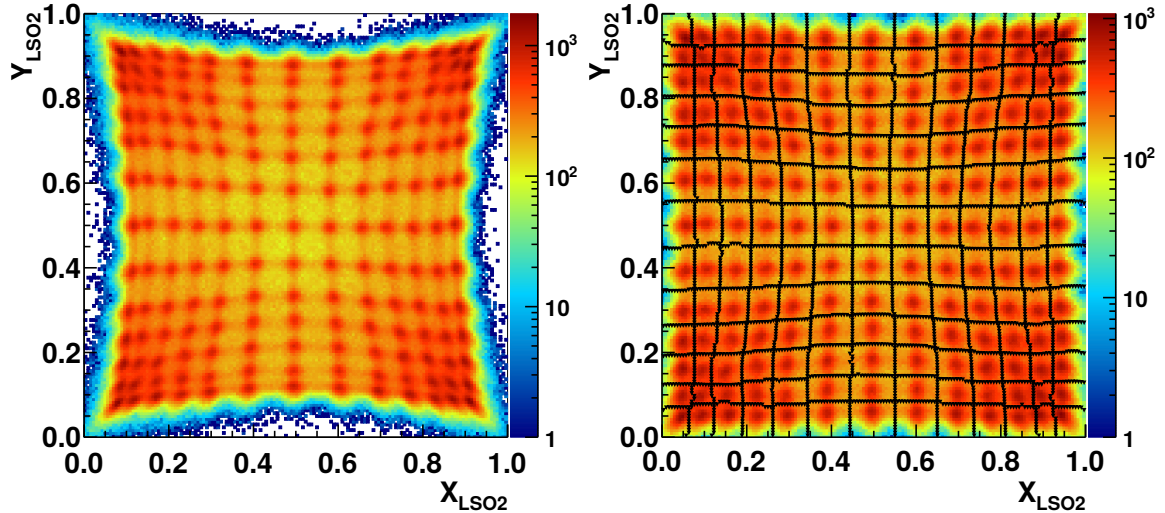


Figure 7. Left: example of a flood map of the LSO2 detector, when irradiated homogeneously by a ^{60}Co source. Right: the flood map distortion correction is applied with the empirical parameters $p = 0.48$, $q = 0.44$, as defined in [65]. The black markers are the pixel boundaries obtained with the automatic segmentation method [64].

Pixel decoding factors One way of determining the resolution with which we can resolve one pixel from the neighbour ones is to measure the peak to valley ratio $P2V$ in the flood map [66]. Alternatively, one could also use as figure of merit the resolution R , defined as the distance to the nearest neighbour pixel centroid divided by the spatial Full Width at Half Maximum (FWHM) Σ of the pixel peak.

6.3 Time calibration

The rise time of the detector signal extracted from the anode (scintillator coupled with PMTs and a custom preamplifier box) is $\sim 5\text{ns}$ for LSO2 and $\sim 10\text{ns}$ for BGO1. This signal is fed to a GSI CF8000 constant fraction discriminator (CFD), whose internal delay line is 2ns and 6ns, respectively. Each anode channel is triggered separately. The CFD module provides also a copy of the input signal, which is delayed and fed to the charge to digital converter. The correction of transit time effects and time walk can be done for each PMT separately. Alternatively, one can use a pixel-wise delay correction and a single time walk correction.

Pixel delay calibration Based on the ELBE experiment [40], where the intrinsic time resolution of the detector can be measured very accurately, we can correct the effect of different transit times for each PMT. Another strategy is to perform this correction for each crystal based on the fast OR signal of the four PMT triggers and the flood map. The time difference between accelerator time stamp and detector trigger is drawn for each crystal with an energy threshold of 2MeV. An automatic procedure locates then the centroid of the timing peak. A reference pixel is chosen, namely the one with the smallest value of the peak centroid. The timing histograms of the rest of the pixels are corrected with an offset in order to match their centroid with the reference one.

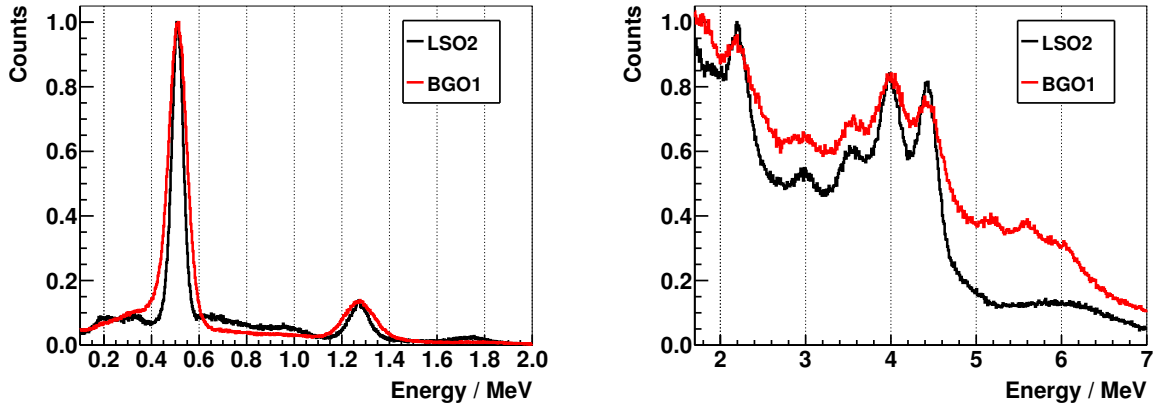


Figure 8. Left: detector response spectrum of the LSO2 detector (black line) for a ^{22}Na source compared to the BGO1 detector (red line). Respective maxima are normalised to one. For LSO2, the intrinsic background is not subtracted as the source activity is significantly higher. Right: analogous spectrum at the prompt gamma ray field at AGOR with 150 MeV protons irradiating a graphite target for the LSO2 and at C230 with 100 MeV impinging a PMMA target for the BGO1. Histogram maximum is normalised to one for the LSO2 detector, the BGO1 spectrum is scaled to match the height of the single escape peak of the LSO2.

Slewing correction Based on the energy over time histograms acquired at ELBE, a time walk correction (also known as slewing correction) is applied as described in [40].

6.4 Error analysis

The measurement of the energy, spatial and time resolution after this complex calibration procedure is done by Gaussian fitting with background subtraction. Although the errors associated to the fitting procedure are well known, they do not reflect the uncertainties of the manual as well as automatic calibration errors one may accumulate at each of these steps. Depending also on the experience of the person calibrating or the number of iterative refinements, the final resolution varies moderately.

Moreover, the energy resolution at different gamma lines is obtained from different measurement campaigns. We use the same detectors, but part of the electronics, the operating voltage, radiation background and temperature are slightly different. This makes a trustworthy estimation of the underlying systematic errors challenging and to some extent subjective. This has to be kept in mind when analysing the results of different experiments in combined graphics.

7. Results and Discussion

7.1 Energy resolution

Figure 8 (left) depicts the detector response spectrum to a ^{22}Na source for each scintillation material. By simple inspection, LSO2 has a better energy resolution. Figure 8 (right) compares two energy spectra of BGO1 and LSO2 at the C230 and AGOR facilities respectively. Both provide a characteristic gamma ray line at 4.44 MeV, which can be seen clearly together with single and double escape peaks. Unfortunately, no absolute efficiency calibration is available at these experiments and the relative height of the peaks of figure 8 cannot be compared quantitatively.

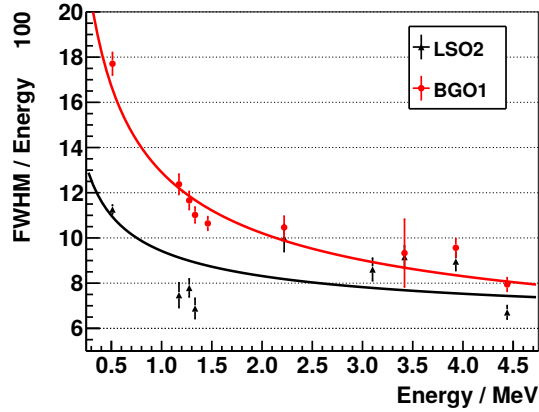


Figure 9. Relative energy resolution of the LSO2 (black line) and BGO1 (red line) block detectors as a function of energy deposit E . The results from various photopeaks obtained at different experiments are combined. The empirical fit to the experimental points is $\text{FWHM}/E = (3.8 \pm 0.3) \% / \sqrt{E/\text{MeV}} + (5.6 \pm 0.3) \%$ for LSO2 and $\text{FWHM}/E = (9.2 \pm 0.5) \% / \sqrt{E/\text{MeV}} + (3.7 \pm 0.4) \%$ for BGO1.

Figure 9 compares the energy resolution at different characteristic gamma ray lines for both block detectors: 0.511 MeV and 1.275 MeV of a ^{22}Na source, 1.173 MeV and 1.333 MeV of a ^{60}Co source, 2.224 MeV from the capture of thermal neutrons on the hydrogen nucleus ($^1\text{H} + n_{\text{th}} \rightarrow ^2\text{H} + \gamma$) at AGOR/C230, and also 4.440 MeV prompt gamma rays as well as its single and double escape peaks.

Note that the measurement of the energy resolution is particularly difficult between 3.4 and 4.4 MeV as photopeak, its Compton edge as well as single and double escape overlap considerably, cf. figure 8 (right), and a multiple Gaussian fit has to be applied together with linear background subtraction. This is also the reason for higher error bars at some of these points.

From figure 9, we can conclude that LSO2 has a better energy resolution than BGO1 in the whole energy range. Nevertheless, the differences are much lower in the high energy range. This points out that LSO2 is significantly better at the PET scenario, below 1 MeV, whereas for the PGI scenario, above 2 MeV, the increase in performance is less accused (below two percentage points), so that the still large material price difference does not correlate necessarily to a much better detector quality.

The reason for the increased performance of BGO material at the PGI range is that the lower light yield is balanced by high gamma ray energies and number of scintillation photons. Consequently, the statistical relative contribution to the energy resolution decreases strongly, whereas the intrinsic contribution (non-linearity effects) dominates and is more or less similar for LSO and BGO scintillation materials (offset parameter in the fit of figure 9).

7.2 Spatial resolution

Figure 10 depicts the flood maps of LSO2 and BGO1 block detectors for different energy ranges of interest. One can clearly identify that the pixel decoding capability increases with the energy range. For higher gamma ray energies, the relative error (Poissonian statistics) is lower. Thus, one can distinguish better between pixels. Note that the higher intensity of some pixels is due to the non uniform irradiation of the crystals: the photons at ELBE are focused (in contrast to 4π emission at

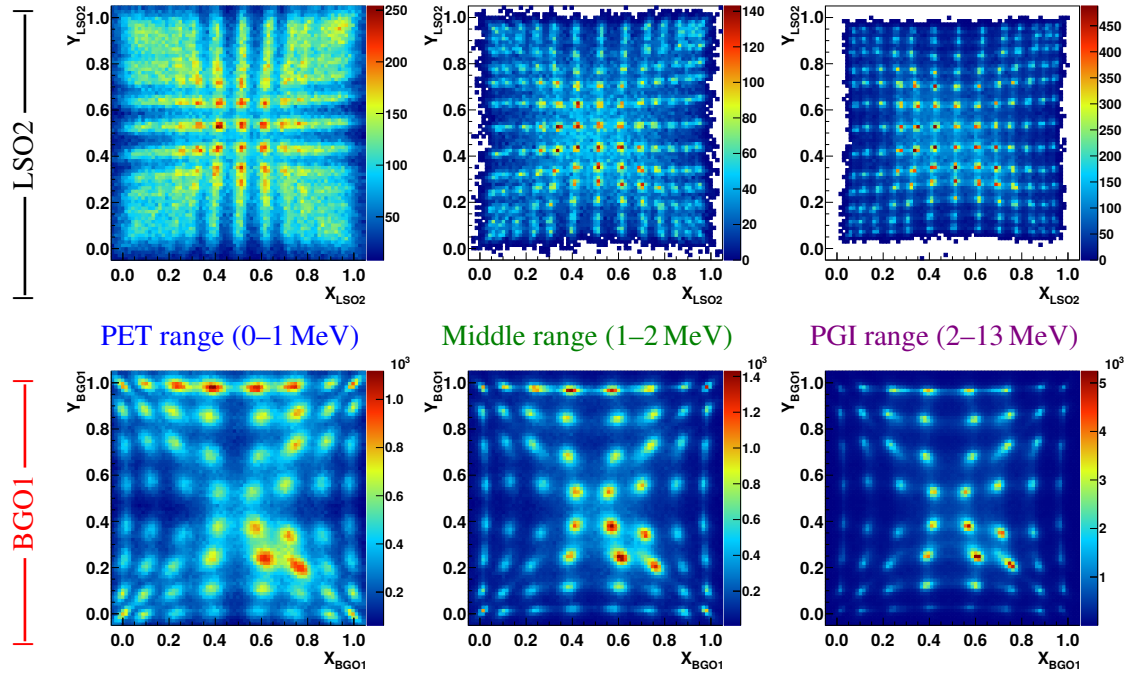


Figure 10. Block detector flood map (top figure: LSO2, middle figure: BGO1) for different energy ranges at the ELBE accelerator (distortion correction applied for LSO2). Non-uniformities are due to the fact that the focused bremsstrahlung beam spot is smaller than the detector size, as well as the different extension (number of bins) of each pixel spot in the map.

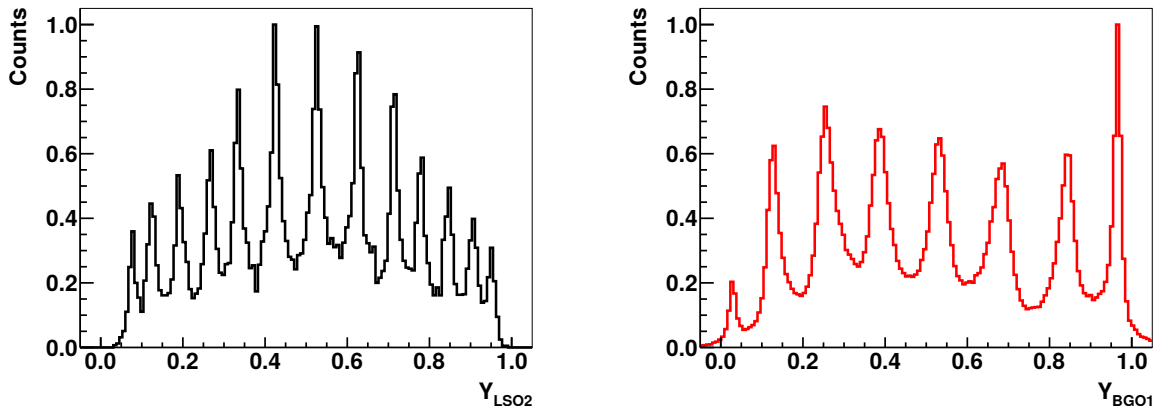


Figure 11. Left: Projection of the flood map depicted in figure 10 (top right) along the fourth crystal column (Y_{LSO2} -axis) of the LSO2 (black line) block detector for the PGI range. Right: analogous projection of the flood map in figure 10 (bottom right) corresponding to the BGO1 (red line) detector and the PGI range. Both: vertical scale is normalised to the respective maximum.

AGOR and C230) and the beam spot is smaller than the block's front face size. Additionally, there are other effects like varying energy threshold depending on pixel location or different amount of bins covered by a certain pixel in the flood map, which explain different intensities in the flood map even with a perfectly homogeneous irradiation.

By simple inspection, BGO1 shows a worse spatial resolution than LSO2 (broader spots in the

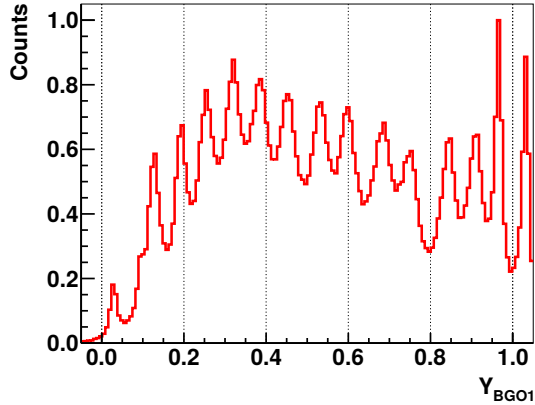


Figure 12. Artificial projection of the flood map of a virtual 8×16 BGO block detector along the fourth crystal column (Y_{Block} -axis). The original projection, which corresponds to BGO1 at the PGI range, cf. figure 11 (right), is cloned and shifted to the right half the average distance between consecutive pixel peaks. Vertical scale is chosen arbitrarily.

map). Nonetheless, the pixels are resolved much sharper for the high energy range. The numerical results presented in table 4 confirm this tendency. In fact, the measured pixel width of BGO1 at the PGI range is similar to that of LSO2 at the PET range, i.e. $\Sigma_{Y(\text{BGO,PGI})} \sim \Sigma_{Y(\text{LSO2,PET})}$.

Detector	LSO2			BGO1		
	Σ	$P2V$	R	Σ	$P2V$	R
PET range	0.05 ± 0.02	2.7 ± 1.1	1.5 ± 0.8	0.08 ± 0.04	1.8 ± 0.4	1.9 ± 0.5
Middle range	0.04 ± 0.02	2.8 ± 1.6	2.1 ± 1.0	0.06 ± 0.02	3.3 ± 1.1	2.5 ± 0.5
PGI range	0.03 ± 0.01	3.7 ± 1.7	2.4 ± 0.9	0.05 ± 0.02	4.4 ± 1.3	3.1 ± 0.8

Table 4. Comparison of the spatial resolution factors of the two scintillation materials at the ELBE experiment. Σ is the width of the pixel peak (in relative crystal coordinates), $P2V$ the peak to-valley ratio and R the resolution. Calculations are made with respect to neighbour pixels of the same crystal column (Y_{Block} -axis), cf. figure 11. The result is averaged over all pixel columns and the error refers to the root mean square. Note that Σ is calculated numerically after applying an iterative background subtraction algorithm [67].

In other words, one could divide the BGO1 block in more pixels per block (as the 13×13 LSO2 matrix), utilise also the same light guide design as of LSO2, cf. figure 2 (right), and still identify each pixel for the PGI range. This is clearly not the case for PET energies, where additional pixels would just overlap in the flood map and one would not be able to separate them any more. To confirm this statement and give some numbers, we model the flood map of a virtual 8×16 BGO block detector by cloning the spatial profile of figure 11 (right), which corresponds to BGO1 at the PGI range, shifting it to the right about half the average distance between consecutive pixel peaks and summing it to the original one. The resulting artificial profile is shown in figure 12.

The figures of merit for the spatial profile depicted in graph 12 are $\Sigma = (0.06 \pm 0.04)$, $P2V = (2.0 \pm 1.0)$ and $R = (1.7 \pm 1.2)$, which means that the performance of a virtual 8×16 BGO block at the PGI range would be close to that of the actual 8×8 BGO1 detector at the PET range. It should be emphasised that this ad hoc procedure simulates more pixels per block detector but does not account for the higher probability of inter-crystal scatter in neighbour (closer) pixels, which

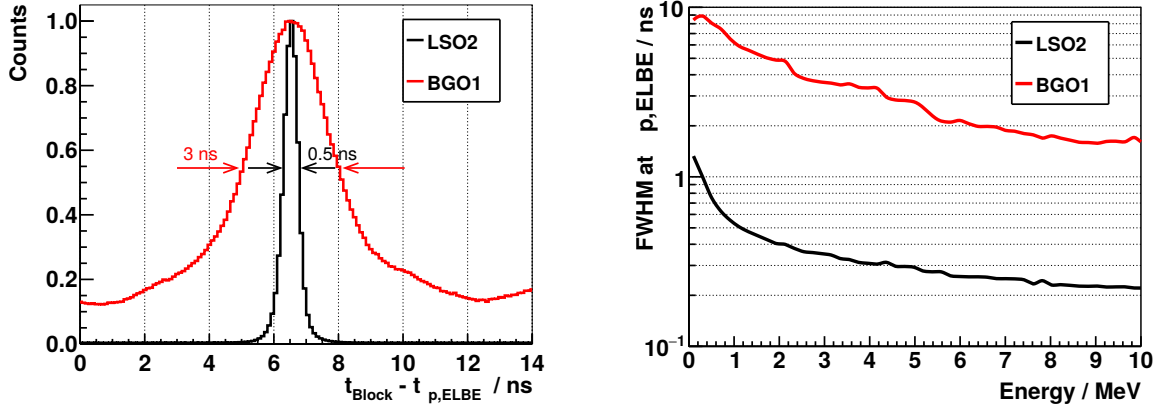


Figure 13. Left: time spectrum of the LSO2 detector (black line) compared to the BGO1 detector (red line) at the ELBE accelerator. The difference between detector signal arrival t_{Block} and closest accelerator micro pulse $t_{\mu\text{p,ELBE}}$ (13 MHz repetition rate, corresponding to 77 ns period) is represented. No energy filter is applied (bremsstrahlung spectrum goes up to 12.5 MeV). Vertical scale is chosen arbitrarily. The arrows mark the FWHM of the time distributions. Right: time resolution (FWHM) for the LSO2 (black line) and BGO1 (red line) block detectors measured at the ELBE accelerator as a function of the released energy. The experimental points are approximately reproduced by the curves $\text{FWHM} = (460 \pm 10) \text{ ps} / \sqrt{E/\text{MeV}} + (80 \pm 5) \text{ ps}$ for LSO2 and $\text{FWHM} = (4900 \pm 500) \text{ ps} / \sqrt{E/\text{MeV}} + (10 \pm 10) \text{ ps}$ for BGO1.

may degrade further the flood map.

7.3 Time resolution

Figure 13 (left) shows the intrinsic time resolution of both blocks at the ELBE accelerator. LSO2 has an excellent time resolution thanks to its high light yield and short decay time. On the other hand, BGO1 has a four times lower light yield and much longer decay time, and can not compete with LSO2 in relative terms, at least with analogue constant fraction trigger.

However, when considering the time resolution as a function of the energy, cf. figure 13 (right), one can see that BGO1 increases its performance significantly, up to 2 ns for high energies, thanks to the higher amplitude of the signals and better determination of the time with the constant fraction discriminator (more statistics, lower relative jitter). By using digital silicon photomultipliers, which can trigger (in principle) on the first photon, a time resolution below 300 ps can be achieved [68] for high photon energies.

In our experiment, it is evident that the LSO2 detector has a significantly better time resolution than BGO1. This is an excluding factor for BGO1 in application fields as time of flight PET or prompt gamma ray timing [59]. For PGI at a clinical accelerator, a good time resolution is also advisable for suppression of radiation background [69] in correlation with accelerator radio frequency. However, the amount of background that can be discriminated depends not only on the detector time resolution, but on the accelerator bunch repetition rate and bunch time spread.

Is then the time resolution obtained with BGO block detectors good enough for PGI in a clinical radiation environment? To give a quantitative answer, we will use the FoM_{BSR} [40], which measures the fraction of background that can be suppressed thanks to timing measurements in a

pulsed accelerator:

$$FoM_{BSR} = 1 - \frac{\sqrt{\Phi_{t,det}^2 + \Phi_{t,bunch}^2}}{\Delta t_{bunch}} \quad (7.1)$$

where $\Phi_{t,det}$ is the detector time resolution (FWHM), $\Phi_{t,bunch}$ the bunch time spread (FWHM) and $\Delta t_{bunch} = f_{bunch}^{-1}$ the time separation between consecutive accelerator bunches (the inverse of the radio frequency).

For the C230 isochronous cyclotron, a widespread accelerator choice in proton therapy centers, $\Delta t_{bunch} = 9.4\text{ns}$ and $\Phi_{t,bunch} \approx 2\text{ns}$ (for 100MeV protons) [26]. In this realistic clinical scenario, the resulting figures of merit for 4MeV prompt gamma rays are $FoM_{BSR,LSO2} = 84\%$ and $FoM_{BSR,BGO1} = 64\%$.

For this reason, the BGO1 performance is acceptable for our goals as long as its time resolution is in the order of magnitude of (or below) the intrinsic proton bunch width (plus gamma emission time). The transit time of protons inside the target (and thus the prompt gamma emission time), which depends on the energy and target composition, is of the order of 1 ns [59]. This effect contributes also to the measured width of the prompt gamma rays in a time spectrum, and implies an additional limit to the background suppression capabilities. Consequently, the BGO1 and LSO2 effective performance is comparable, as the significant difference in time resolution is shadowed by the bunch time spread and transit time. Rather than the detector time resolution itself, two other material features are of great significance: the decay time and the intrinsic radioactivity.

The decay time of BGO (7.5 times longer than LSO) is not appropriate for very high counting rate application. As a rule of thumb, the count rate limit with manageable pile up is given by an average impulse separation of ten times the decay constant: 300kcps for BGO and 2.5Mcps for LSO. What is the expected rate in a realistic clinical scenario for a BGO block detector? At $\sim 2\text{nA}$ (10^{10} protons per second) instantaneous beam current [15], assuming for simplicity a yield of 0.15 prompt gamma rays per proton, a gamma ray attenuation of $\sim 40\%$ in the patient [70] and the BGO1 block at 30cm distance with interaction efficiency $\epsilon_D \approx 50\%$ [43], we score $\epsilon_{p\gamma} \simeq 10^{-4}$ gamma rays per proton. The resulting detector load (during effective beam delivery) is $\sim 1\text{Mcps}$. This implies that BGO blocks with a smaller area (one third) should be deployed for this application, or (alternatively) that the distance from block to beam axis should be increased up to 55cm, to keep the count rate around the $\sim 300\text{kcps}$ limit. It is worthwhile to mention that such detector rates are also challenging for the electronics, data acquisitions and real-time processing.

On the other hand, LSO has a larger afterglow and high intrinsic radioactivity under 1MeV due to ^{176}Lu , which may lead to a considerable amount of false coincidences in a Compton camera as discussed in subsection 4.2.

8. Conclusions

Prompt gamma imaging is a reasonable approach for reconstructing the particle range in ion beam therapy. A Compton camera for these gamma ray energies is very challenging, as the underlying detector materials need to cope with demanding and diverse prerequisites at the same time. To support the design and development of a Compton camera, we need an experimental exploration of the detector behaviour in clinical-like radiation environments concerning energy spectroscopy,

spatial resolution and timing. We compare at three different research accelerators two scintillation materials which are promising candidates for the absorber plane: BGO and LSO.

LSO has an overall better performance, especially concerning timing resolution, but BGO closes the gap in the PGI range, as the high number of scintillation photons compensates for its lower light yield. The higher photofraction, absence of intrinsic radioactivity and much lower price make BGO a promising alternative material for the absorber, with an outcome comparable to LSO for the intended application. In other words, for the same price, a bigger BGO camera could be built without significant quality loss. Indeed, a 13×13 BGO block detector, as the LSO, might be constructed to improve its spatial resolution.

In conclusion, the statement about the superiority of LSO in the PET scenario can not be directly transcribed to PGI applications. The experimental detector characterization reveals the suitability of BGO as absorber of a clinical Compton camera with a superior cost-effectiveness ratio.

Acknowledgments

This work is supported by the German Federal Ministry of Education and Research (BMBF-03Z1NN12) and the European Commission (ENTERVISION FP7 Grant Agreement N. 264552 and IA-ENSAR FP7 contract N. RII3-CT-2010-262010). The authors like to thank M. Berthel^a, A. Dreyer^a, as well as the crew of the ELBE, AGOR and OncoRay accelerators for the excellent support. We also thank Dr. Hartwig Newiger and Dr. Maciej Kapusta from Siemens Healthcare Molecular Imaging for the information about the block detector construction and geometry.

References

- [1] R. R. Wilson, *Radiological use of fast protons*, *Radiology* **47-5**:487 (1946).
- [2] M. Goitein and M. Jermann, *The Relative Costs of Proton and X-ray Radiation Therapy*, *Clinical Oncology* **15-1**:S37–S50 (2003).
- [3] T. Freeman, *Will protons gradually replace photons?*, *Medical Physics Web* **August-22** (2012).
- [4] J. Deasy, *ICRU Report 49, Stopping Powers and Ranges for Protons and Alpha Particles*, *Medical Physics* **21-5** (1994).
- [5] P. Andreo, *On the clinical spatial resolution achievable with protons and heavier charged particle radiotherapy beams*, *Phys. Med. Biol.* **54-11**:N205 (2009).
- [6] F. Albertini, E. B. Hug, and A. J. Lomax, *Is it necessary to plan with safety margins for actively scanned proton therapy?*, *Phys. Med. Biol.* **56-14**:4399 (2011).
- [7] C. G. Orton and W. R. Hendee, eds., *Controversies in Medical Physics: a Compendium of Point/Counterpoint Debates*, pp. 110–123. American Association of Physicists in Medicine, 2008.
- [8] A.-C. Knopf and A. Lomax, *In vivo proton range verification: a review*, *Phys. Med. Biol.* **58-15**:R131 (2013).
- [9] C.-H. Min, C. H. Kim, M.-Y. Youn, and J.-W. Kim, *Prompt gamma measurements for locating the dose falloff region in the proton therapy*, *Applied Physics Letters* **89-18** (2006).

- [10] F. Janssen, G. Landry, P. C. Lopes, G. Dedes, J. Smeets, D. R. Schaart, K. Parodi, and F. Verhaegen, *Factors influencing the accuracy of beam range estimation in proton therapy using prompt gamma emission*, *Phys. Med. Biol.* **59-15**:4427 (2014).
- [11] K. S. Seo, C. H. Kim, and J. W. Kim, *Comparison of Titanium Hydride (TiH₂) and Paraffin as Neutron Moderator Material in a Prompt Gamma Scanning System*, *J. Korean Phys. Soc.* **48-4**:855 (2006).
- [12] J. M. Verburg, M. Testa, and J. Seco, *Range verification of passively scattered proton beams using prompt gamma-ray detection*, *Phys. Med. Biol.* **60-3**:1019 (2015).
- [13] M. Pinto, D. Dauvergne, N. Freud, J. Krimmer, J. M. Letang, C. Ray, F. Roellinghoff, and E. Testa, *Design optimisation of a TOF-based collimated camera prototype for online hadrontherapy monitoring*, *Phys. Med. Biol.* **59-24**:7653 (2014).
- [14] J. Smeets, F. Roellinghoff, D. Prieels, F. Stichelbaut, A. Benilov, P. Busca, C. Fiorini, R. Peloso, M. Basilavecchia, T. Frizzi, J. C. Dehaes, and A. Dubus, *Prompt gamma imaging with a slit camera for real-time range control in proton therapy*, *Phys. Med. Biol.* **57-11**:3371 (2012).
- [15] I. Perali, A. Celani, L. Bombelli, C. Fiorini, F. Camera, E. Clementel, S. Henrotin, G. Janssens, D. Prieels, F. Roellinghoff, J. Smeets, F. Stichelbaut, and F. V. Stappen, *Prompt gamma imaging of proton pencil beams at clinical dose rate*, *Phys. Med. Biol.* **59-19**:5849 (2014).
- [16] M. Priegnitz, S. Helmbrecht, G. Janssens, I. Perali, J. Smeets, F. V. Stappen, E. Sterpin, and F. Fiedler, *Measurement of prompt gamma profiles in inhomogeneous targets with a knife-edge slit camera during proton irradiation*, *Phys. Med. Biol.* **60-12**:4849 (2015).
- [17] A. H. Compton, *A Quantum Theory of the Scattering of X-rays by Light Elements*, *Phys. Rev.* **21-5**:483–502 (1923).
- [18] H. Seo, J. H. Park, A. Ushakov, C. H. Kim, J. K. Kim, J. H. Lee, C. S. Lee, and J. S. Lee, *Experimental performance of double-scattering Compton camera with anthropomorphic phantom*, *Journal of Instrumentation* **6-01**:C01024 (2011).
- [19] J. Krimmer, J.-L. Ley, C. Abellan, J.-P. Cachemiche, L. Caponetto, X. Chen, M. Dahoumane, D. Dauvergne, N. Freud, B. Joly, D. Lambert, L. Lestand, J. Létang, M. Magne, H. Mathez, V. Maxim, G. Montarou, C. Morel, M. Pinto, C. Ray, V. Reithinger, E. Testa, and Y. Zoccarato, *Development of a Compton camera for medical applications based on silicon strip and scintillation detectors*, *Nucl. Inst. & Meth. in Phys. Res. A* **0** (2014).
- [20] G. Llosá, J. Cabello, S. Callier, J. Gillam, C. Lacasta, M. Rafecas, L. Raux, C. Solaz, V. Stankova, C. de La Taille, M. Trovato, and J. Barrio, *First Compton telescope prototype based on continuous LaBr₃-SiPM detectors*, *Nucl. Inst. & Meth. in Phys. Res. A* **718-0**:130–133 (2013).
- [21] P. Thirof, C. Lang, S. Aldawood, H. v.d. Kolff, L. Maier, D. Schaart, and K. Parodi, *Development of a Compton Camera for Online Range Monitoring of Laser-Accelerated Proton Beams via Prompt-Gamma Detection*, *EPJ Web of Conferences* **66-11036** (2014).
- [22] T. Kormoll, F. Fiedler, S. Schöne, J. Wüstemann, K. Zuber, and W. Enghardt, *A Compton imager for in-vivo dosimetry of proton beams - A design study*, *Nucl. Inst. & Meth. in Phys. Res. A* **626-627-0**:114–119 (2011).
- [23] S. Kurosawa, H. Kubo, K. Ueno, S. Kabuki, S. Iwaki, M. Takahashi, K. Taniue, N. Higashi, K. Miuchi, T. Tanimori, D. Kim, and J. Kim, *Prompt gamma detection for range verification in proton therapy*, *Current Applied Physics* **12-2**:364–368 (2012).

- [24] M. McCleskey, W. Kaye, D. Mackin, S. Beddar, Z. He, and J. Polf, *Evaluation of a multistage CdZnTe Compton camera for prompt γ imaging for proton therapy*, *Nucl. Inst. & Meth. in Phys. Res. A* **785-0**:163–169 (2015).
- [25] J. M. Verburg and J. Seco, *Proton range verification through prompt gamma-ray spectroscopy*, *Phys. Med. Biol.* **59-23**:7089 (2014).
- [26] F. Hueso-González, W. Enghardt, F. Fiedler, C. Golnik, G. Janssens, J. Petzoldt, D. Prieels, M. Priegnitz, K. E. Römer, J. Smeets, F. V. Stappen, A. Wagner, and G. Pausch, *First test of the prompt gamma ray timing method with heterogeneous targets at a clinical proton therapy facility*, *Physics in Medicine and Biology* **60-16**:6247 (2015).
- [27] W. D. Newhauser and R. Zhang, *The physics of proton therapy*, *Phys. Med. Biol.* **60-8**:R155 (2015).
- [28] D. Robertson, J. C. Polf, S. W. Peterson, M. T. Gillin, and S. Beddar, *Material efficiency studies for a Compton camera designed to measure characteristic prompt gamma rays emitted during proton beam radiotherapy*, *Phys. Med. Biol.* **56-10**:3047 (2011).
- [29] M.-H. Richard, *Design study of a Compton camera for prompt- γ imaging during ion beam therapy*, *PhD thesis, Université Claude Bernard Lyon 1* (2012).
- [30] T. Kormoll, *A Compton Camera for In-vivo Dosimetry in Ion-beam Radiotherapy*, *PhD thesis, Technische Universität Dresden* (2012).
- [31] J. L. Humm, A. Rosenfeld, and A. Del Guerra, *From PET detectors to PET scanners*, *European Journal of Nuclear Medicine and Molecular Imaging* **30-11**:1574–1597 (2003).
- [32] R. Mao, L. Zhang, and R.-Y. Zhu, *LSO/LYSO Crystals for Future HEP Experiments*, *Journal of Physics: Conference Series* **293-1**:12004 (2011).
- [33] L. Zhang, R. Mao, S. Wang, F. Yang, and R.-Y. Zhu, *A study on radiation hardness of BGO crystals*, *Nuclear Science Symposium and Medical Imaging Conference (NSS/MIC), 2012 IEEE* (2012).
- [34] C. L. Melcher, *Scintillation crystals for PET*, *Journal of Nuclear Medicine* **41-6**:1051–5 (2000).
- [35] R. Ramirez, W.-H. Wong, S. Kim, H. Baghaei, H. Li, Y. Wang, Y. Zhang, S. Liu, and J. Liu, *A comparison of BGO, GSO, MLS, LGSO, LYSO and LSO scintillation materials for high-spatial-resolution animal PET detectors*, *Nuclear Science Symposium and Medical Imaging Conference (NSS/MIC), 2005 IEEE Conf. Rec.* **5** (2005).
- [36] S. Weber, D. Christ, M. Kurzeja, R. Engels, G. Kemmerling, and H. Halling, *Comparison of LuYAP, LSO, and BGO as scintillators for high resolution PET detectors*, *Nuclear Science, IEEE Transactions on* **50-5**:1370–1372 (2003).
- [37] T. Szczesniak, M. Kapusta, M. Moszynski, M. Grodzicka, M. Szawlowski, D. Wolski, J. Baszak, and N. Zhang, *MPPC Arrays in PET Detectors With LSO and BGO Scintillators*, *Nuclear Science, IEEE Transactions on* **60-3**:1533–1540 (2013).
- [38] A. Gektin, N. Shiran, A. Belsky, and A. Vasil'ev, *Luminescence fundamental limits for alkali halide scintillators*, *3d SUCCESS International Scientific Workshop* (2012).
- [39] J. M. Verburg, K. Riley, T. Bortfeld, and J. Seco, *Energy- and time-resolved detection of prompt gamma-rays for proton range verification*, *Phys. Med. Biol.* **58-20**:L37 (2013).
- [40] F. Hueso-González, C. Golnik, M. Berthel, A. Dreyer, W. Enghardt, F. Fiedler, K. Heidel, T. Kormoll, H. Rohling, S. Schöne, R. Schwengner, A. Wagner, and G. Pausch, *Test of Compton camera components for prompt gamma imaging at the ELBE bremsstrahlung beam*, *JINST* **9-05**:P05002 (2014).

- [41] T. Kormoll, C. Golnik, S. Akhmadaliev, D. Bemmerer, J. Borany, F. Fiedler, F. Hueso-Gonzalez, K. Heidel, M. Kempe, H. Rohling, K. Schmidt, S. Schone, L. Wagner, and G. Pausch, *Compton imaging in a high energetic photon field*, *Nuclear Science Symposium and Medical Imaging Conference (NSS/MIC)*, 2013 *IEEE M19-3*.
- [42] *Review of Particle Physics*, *Physical Review D* **86-1:010001** (2012).
- [43] M. Berger, J. Hubbell, S. S. abd J. Chang, J. Coursey, R. Sukumar, D. Zucker, and K. Olsen, *XCOM: Photon Cross Section Database*, *NIST Standard Reference Database 8 (XGAM)*, NIST - (2010).
- [44] R. Mao, L. Zhang, and R.-Y. Zhu, *Crystals for the HHCAL Detector Concept*, *Journal of Physics: Conference Series* **404-1:012029** (2012).
- [45] S. Derenzo, M. Weber, W. Moses, and C. Dujardin, *Measurements of the intrinsic rise times of common inorganic scintillators*, *Nuclear Science, IEEE Transactions on* **47-3:860–864** (2000).
- [46] D. Bailey, D. Townsend, P. Valk, and M. Maisey, eds., *Physics and Instrumentation in PET*, pp. 13–39. Springer London, 2005.
- [47] P. Crespo, *Optimization of in-beam Positron Emission Tomography for monitoring heavy ion tumor therapy*, *PhD thesis, Technische Universität Dresden* (2006).
- [48] A. Nassalski, M. Kapusta, T. Batsch, D. Wolski, D. Mockel, W. Enghardt, and M. Moszyński, *Comparative study of scintillators for PET/CT detectors*, *Nuclear Science Symposium and Medical Imaging Conference (NSS/MIC)*, 2005 *IEEE Conf. Rec.* **5** (2005).
- [49] K. Roemer, G. Pausch, D. Bemmerer, M. Berthel, A. Dreyer, C. Golnik, F. Hueso-González, T. Kormoll, J. Petzoldt, H. Rohling, P. Thierolf, A. Wagner, L. Wagner, D. Weinberger, and F. Fiedler, *Characterization of Scintillator Crystals for Usage as Prompt Gamma Monitors in Particle Therapy*, submitted to *JINST* - (2015).
- [50] M. Moszyński, C. Gresset, J. Vacher, and R. Odru, *Timing properties of BGO scintillator*, *Nucl. Inst. & Meth. in Phys. Res.* **188-2:403–409** (1981).
- [51] R. Yao, T. Ma, and Y. Shao, *Effects of LSO detector intrinsic radioactivity on SPECT imaging*, *Nuclear Science Symposium and Medical Imaging Conference (NSS/MIC)*, 2007 *IEEE Conf. Rec.*, **M11-67**.
- [52] M. Berger, J. Coursey, M. Zucker, and J. Chang, *ESTAR, PSTAR, and ASTAR: Computer Programs for Calculating Stopping-Power and Range Tables for Electrons, Protons, and Helium Ions*, NIST - (2005).
- [53] P. Dorenbos, J. de Haas, and C. van Eijk, *Non-proportionality in the scintillation response and the energy resolution obtainable with scintillation crystals*, *Nuclear Science, IEEE Transactions on* **42-6:2190–2202** (1995).
- [54] R.-Y. Zhu, *Fast Crystals for Forward Calorimeter Upgrade at HL-LHC*, *CMS Forward Calorimetry Taskforce Meeting*, 2012 **Talk**.
- [55] A. Chatzioannou, Q. Bao, and N. Karakatsanis, *System sensitivity in preclinical small animal imaging*, *Biomedical Imaging: From Nano to Macro*, 2008. *ISBI 2008. 5th IEEE International Symposium on* (2008).
- [56] P. G. Ortega, I. Torres-Espallardo, F. Cerutti, A. Ferrari, J. E. Gillam, C. Lacasta, G. Llosá, J. F. Oliver, P. R. Sala, P. Solevi, and M. Rafecas, *Noise evaluation of Compton camera imaging for proton therapy*, *Phys. Med. Biol.* **60-5:1845** (2015).
- [57] S. W. Peterson, D. Robertson, and J. Polf, *Optimizing a three-stage Compton camera for measuring prompt gamma rays emitted during proton radiotherapy*, *Phys. Med. Biol.* **55-22:6841** (2010).

- [58] R. Brun and F. Rademakers, *ROOT - An object oriented data analysis framework*, *Nucl. Inst. & Meth. in Phys. Res. A* **389-1-2**:81–86 (1997).
- [59] C. Golnik, F. Hueso-González, A. Müller, P. Dendooven, W. Enghardt, F. Fiedler, T. Kormoll, K. Roemer, J. Petzoldt, A. Wagner, and G. Pausch, *Range assessment in particle therapy based on prompt γ -ray timing measurements*, *Phys. Med. Biol.* **59-18**:5399 (2014).
- [60] R. Schwengner, R. Beyer, F. Döna, E. Grosse, A. Hartmann, A. Junghans, S. Mallion, G. Rusev, K. Schilling, W. Schulze, and A. Wagner, *The photon-scattering facility at the superconducting electron accelerator ELBE*, *Nucl. Inst. & Meth. in Phys. Res. A* **555-1-2**:211–219 (2005).
- [61] S. Brandenburg, R. Ostendorf, M. Hofstee, H. Kiewiet, and H. Beijers, *The irradiation facility at the AGOR cyclotron*, *Nucl. Inst. & Meth. in Phys. Res. B* **261-1-2**:82–85 (2007).
- [62] A. Schumann, J. Petzoldt, P. Dendooven, W. Enghardt, C. Golnik, F. Hueso-González, T. Kormoll, G. Pausch, K. Roemer, and F. Fiedler, *Simulation and experimental verification of prompt gamma-ray emissions during proton irradiation*, *Physics in Medicine and Biology* **60-10**:4197 (2015).
- [63] K. Stonger and M. Johnson, *Optimal calibration of PET Crystal position maps using Gaussian mixture models*, *Nuclear Science, IEEE Transactions on* **51-1**:85–90 (2004).
- [64] Q. Wei, X. Li, T. Ma, S. Wang, T. Dai, P. Fan, Y. Yunhan, Y. Jin, and Y. Liu, *A neighborhood standard deviation based algorithm for generating PET crystal position maps*, *Nuclear Science Symposium and Medical Imaging Conference (NSS/MIC), 2013 IEEE* **M18-45**.
- [65] S. Cui, A. Vandenbroucke, M. Bieniosek, and C. Levin, *General spatial distortion correction method for solid-state position sensitive detectors in PET*, *Nuclear Science Symposium and Medical Imaging Conference (NSS/MIC), 2013 IEEE* **M03-6**.
- [66] R. A. Ramirez, Y. Zhang, S. Liu, H. Li, H. Baghaei, S. An, C. Wang, M.-L. Jan, and W.-H. Wong, *A Lower-Cost High-Resolution LYSO Detector Development for Positron Emission Mammography (PEM)*, *IEEE Transactions on Nuclear Science* **56-5**:2621–2627 (2009).
- [67] C. Ryan, E. Clayton, W. Griffin, S. Sie, and D. Cousens, *SNIP, a statistics-sensitive background treatment for the quantitative analysis of PIXE spectra in geoscience applications*, *Nucl. Inst. & Meth. in Phys. Res. B* **34-3**:396–402 (1988).
- [68] J. Petzoldt, K. Römer, T. Kormoll, M. Berthel, A. Dreyer, W. Enghardt, F. Fiedler, F. Hueso-González, C. Golnik, T. Kirschke, A. Wagner, and G. Pausch, *Fast Timing with BGO (and other Scintillators) on Digital Silicon Photomultipliers for Prompt Gamma Imaging*, *Nuclear Science Symposium and Medical Imaging Conference (NSS/MIC), 2014 IEEE Conf. Rec.*, **N48-4**.
- [69] A. K. Biegun, E. Seravalli, P. C. Lopes, I. Rinaldi, M. Pinto, D. C. Oxley, P. Dendooven, F. Verhaegen, K. Parodi, P. Crespo, and D. R. Schaart, *Time-of-flight neutron rejection to improve prompt gamma imaging for proton range verification: a simulation study*, *Phys. Med. Biol.* **57-20**:6429 (2012).
- [70] J. H. Hubbell and S. M. Seltzer, *Tables of X-Ray Mass Attenuation Coefficients and Mass Energy-Absorption Coefficients from 1 keV to 20 MeV for Elements Z = 1 to 92 and 48 Additional Substances of Dosimetric Interest*, *NIST* - (2004).